Hyperbolic Mode Control with Boron Nitride Nanotubes and Its Impact on Near-field Radiative Heat Transfer

by

Vishwa Krishna Rajan

A Thesis Presented in Partial Fulfillment
of the Requirements for the Degree
Master of Science

Approved June 2022 by
Graduate Supervisory Committee:

Liping Wang, Chair
Patrick Phelan
Robert Wang

ARIZONA STATE UNIVERSITY

August 2022

ABSTRACT

Radiation heat transfer can surpass blackbody limit when distance between the hot emitter and cold receiver is less than the characteristic wavelength of electromagnetic radiation. The enhanced radiation heat transfer achieved is also called near-field radiation heat transfer. Several theoretical and experimental studies have demonstrated enhancement in near-field radiation heat transfer for isotropic materials such as silicon carbide (SiC), undoped and doped Si. The enhancement achieved however is narrow-banded. Significant improvement in radiation heat transfer is necessary to satisfy some of the energy demands. So, there is a growing interest to use hyperbolic materials because of its enhancement due to propagating modes. The main objective of the current thesis project is to investigate the control of hyperbolic bands using boron nitride nanotubes (nanostructure of hexagonal boron nitride) for near-field radiative heat transfer.

Optical properties of boron nitride nanotubes are calculated using Maxwell-Garnet's effective medium theory and its corresponding hyperbolic bands are identified. It is observed that the boron nitride nanotubes have only one hyperbolic band located at higher frequencies. Preliminary comparisons of the near-field radiative heat flux calculations with literature are performed using a more general 4×4 transfer matrix method. Due to its high computational time, anisotropic thin film optics is used to calculate near-field radiative heat transfer. Factors contributing to enhancement is investigated. In the end, Spectral allocation ratio, the ratio of heat flux contributed from higher frequencies to the heat flux contributed from lower frequencies is calculated to assess the contribution of each hyperbolic band to total heat flux.

ACKNOWLEDGEMENTS

I thank my advisor and thesis advisor Dr. Liping Wang for his valuable guidance to carry out this project. I would also like to thank my committee members Dr. Patrick Phelan and Dr. Robert Wang for taking their valuable time to serve on my committee. Special mention to few of my current and formed lab mates-Rajagopalan Ramesh, Chen and Jeremy chao. Finally, I would like to thank my friends and family for their constant support during my thesis

TABLE OF CONTENTS

Page

CHAPTER Page

LIST OF TABLES

Table Page

LIST OF FIGURES

Figure Page

Figure Page

1 INTRODUCTION

1.1 Planck's Law of Blackbody Radiation

Blackbody emits and absorbs maximum amount of spectral radiative energy at a given temperature. Planck's law describes the spectral power emitted by a blackbody at distinct energy levels [1]. Mathematically in terms of wavelength, it is represented as

$$E_{b\lambda}(\lambda, T) = \frac{C_1}{\lambda^5 \left[e^{\frac{C_2}{\lambda T}} - 1 \right]} \tag{1-1}$$

where $C_1 = 2\pi h c_o^2 = 3.7418 \times 10^{-16} W\, m^2$, $C_2 = \frac{h c_o}{k_b} = 14{,}388\, \mu m\, K$, h is Planck's constant, c_o is the speed of light and k_b is the Boltzmann's constant.

Figure 1.1 shows the spectrum of Planck's law of blackbody radiation. It can be observed that the peak in spectral emissive power shifts to lower wavelengths at higher temperatures. The peak in spectral heat flux can be obtained by differentiating equation (1-1) and equating to zero. Doing this will give,

$$\lambda_{max} T = 2898\, \mu m\, K \tag{1-2}$$

Equation (1-2) is the well-known Wien's displacement law. Equation (1-1) can also be written in terms of wavenumber $\left(\eta = \frac{1}{\lambda}\right)$ and frequency $\left(\nu = \frac{c_o}{\lambda}\right)$ based on the relation,

$$-E_{b\lambda} d\lambda = E_{b\nu} d\nu = E_{b\eta} d\eta \tag{1-3}$$

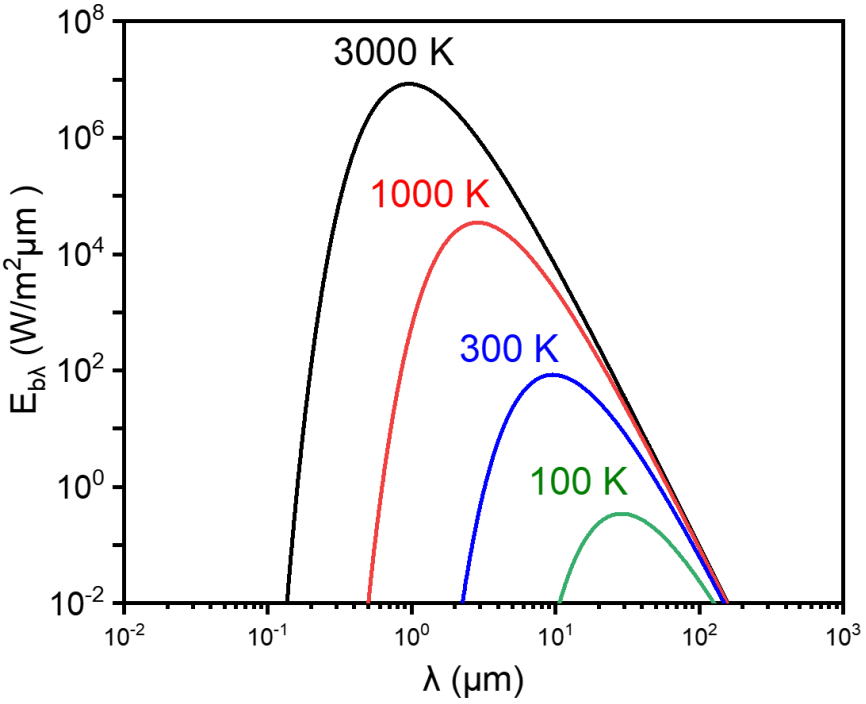

Figure 1.1 Spectral Emissive Power of Blackbody Based on Planck's Law

The total blackbody emissive power can be obtained by integrating (1-1) over the entire wavelength spectrum and the total emissive power is obtained as,

$$E_b = \int_0^\infty E_{b\lambda}(\lambda, T)d\lambda = \sigma T^4 \tag{1-4}$$

where $\sigma = 5.67 \times 10^{-8} \frac{W}{m^2 K^4}$ is the Stefan-Boltzmann's constant. Equation (1-4) is famous Stefan-Boltzmann's law which depends only on the temperature of the blackbody.

1.2 Near-field Thermal Radiation

For many years, Planck's law is established as a ceiling for radiative heat transfer between two bodies. However, Planck's law is valid only when the perpendicular distance between two bodies d is very much greater than the characteristic wavelength of

electromagnetic radiation. When d is comparable or less than the characteristic wavelength, radiative heat transfer greater than the Planck's law of blackbody radiation is achieved [2,3]. This phenomenon is called near-field thermal radiation.

Figure 1.2 shows the schematic illustrating the mechanism involved in near-field thermal radiation. When a wave approaches from an optically denser medium to a rarer medium, the wave will get reflected internally when the incidence angle is greater than the critical angle. There exists an exponentially decaying evanescent wave in the rarer medium which does not contribute to energy transport when the separation distance d is greater than the characteristic wavelength. When two objects are placed relatively closer such that separation distance is less than the characteristic wavelength, energy is transported to other medium by evanescent waves. This phenomenon is also described as photon tunnelling or frustrated total internal reflection.

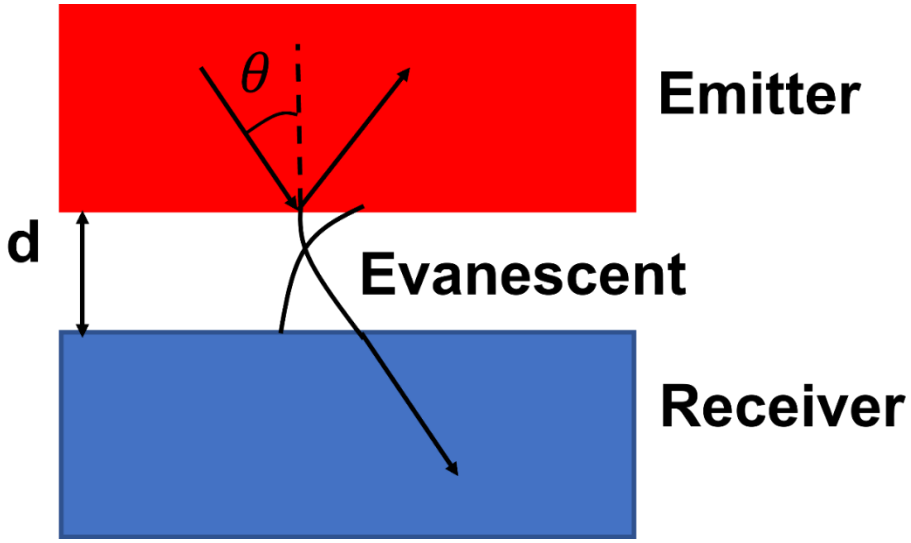

Figure 1.2 Schematic Illustrating Near-field Thermal Radiation

1.3 Hyperbolic Materials

Near-field radiation heat transfer (NFRHT) is widely used in applications such as near-field thermophotovoltaics[4–7], radiative cooling of nanostructures[8], non-contact refrigeration[9], thermal transistor[10] and thermal rectification[11,12]. Enhancement in NFRHT in isotropic materials generally offers narrow-banded surface mode enhancements due to excitation of surface plasmon/phonon polaritons [13–20] (interaction of electromagnetic waves with charges/optical phonons). Significant improvement in NFRHT is required to satisfy the demands of the aforementioned applications. Hyperbolic materials are materials that show hyperbolic or infinite dispersion occupying higher wavevector values. The short background of hyperbolic materials is described below.

The dielectric function tensor of a uniaxial tensor can be represented as,

$$\varepsilon = \begin{bmatrix} \varepsilon_{\parallel} & 0 & 0 \\ 0 & \varepsilon_{\parallel} & 0 \\ 0 & 0 & \varepsilon_{\perp} \end{bmatrix} \tag{1-5}$$

where ∥ and ⊥ indicates component of dielectric function parallel and perpendicular to surface of the material respectively. For extraordinary waves, the iso-frequency surface is given by,

$$\frac{{k_x}^2 + k_y^2}{\varepsilon_{\perp}} + \frac{{k_z}^2}{\varepsilon_{||}} = \frac{\omega^2}{c^2} \tag{1-6}$$

The above iso-frequency surface will show hyperbolic dispersion when signs of $Re(\varepsilon_{\perp})$ and $Re(\varepsilon_{\parallel})$ are opposite.When $Re(\varepsilon_{\perp})$ <0 and $Re(\varepsilon_{\parallel})$ >0, the material shows type I hyperbolic dispersion and iso-frequency surface will be a two-sheeted hyperboloid. When sign of $Re(\varepsilon_{\perp})$ >0 and $Re(\varepsilon_{\parallel})$ <0, the material shows type II hyperbolic dispersion and

iso-frequency surface will be a one-sheeted hyperboloid. Figure 1.3 (a) shows a two-sheeted hyperboloid drawn for $\varepsilon_{\perp}\frac{\omega^2}{c^2} = -0.5$ and $\varepsilon_{||}\frac{\omega^2}{c^2} = 0.4$ and Figure 1.3 (b) shows a one-sheeted hyperboloid drawn for $\varepsilon_{\perp}\frac{\omega^2}{c^2} = 0.5$ and $\varepsilon_{||}\frac{\omega^2}{c^2} = -0.3$. Generally, if the occupied wavevector values lie on the hyperboloid,there will be significant enhancement in NFRHT due to its infinite dispersion.

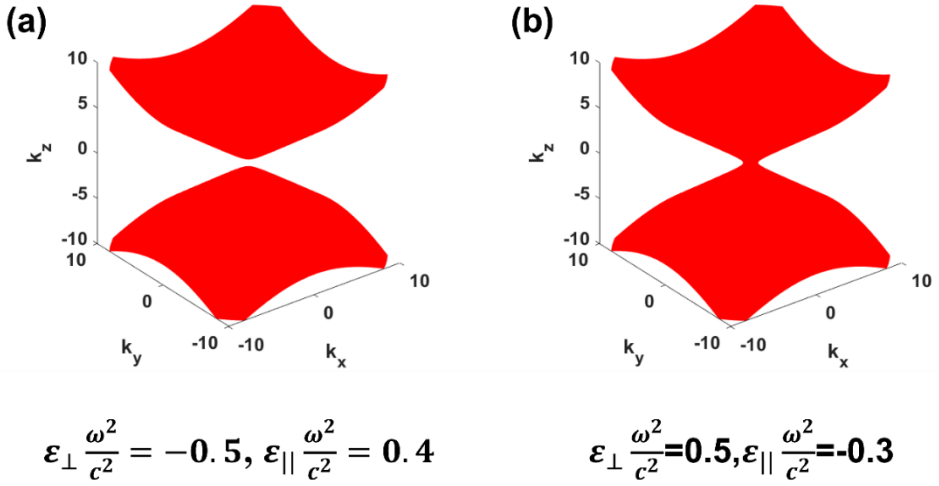

Figure 1.3 Iso-frequency Contours of Hyperbolic Materials (a) Type I (b) Type II

1.4 Literature Review on NFRHT Between Hyperbolic Materials

Hyperbolic materials can be categorized either as natural hyperbolic material or artificial hyperbolic material based on its availability. NFRHT enhancement due to hyperbolic modes was demonstrated between natural hyperbolic materials such as hBN[21–23], calcite[24], α- MoO_3[25]. Also, NFRHT was investigated between different structured materials such as graphene covered natural hyperbolic materials[21],[26–28] gratings[29,30] multilayers[29],[31,32] and nanowire or nano tube arrangements[29],[33–35]. Graphene covered natural hyperbolic materials gave a broadband enhancement in heat flux due to coupling of surface plasmons in graphene and hyperbolic modes in hyperbolic

material [21],[26–28]. Liu et al [29] created nanostructures such as nanowire, nanohole, grating and multilayers displaying hyperbolic property from doped Si and studied the NFRHT for each structure. It was shown that doped Si nanowire and nanoholes showed more enhancement than bulk over one order of magnitude. Shen et al[30] investigated the NFRHT theoretically between grating structures of natural anisotropic material graphite. Graphite grating structure discussed in ref. [30] supported type I hyperbolic dispersion due to which there was 5.5-fold more spectral heat flux than the normal graphite plate configuration. Guo et. al[31] and Biehs et. al[32] studied the NFRHT heat flux between multilayer structures with SiC and SiO_2 stacked on top of one another, thus displaying hyperbolic property. Nanowire arrangement formed out of SiC[34] also showed hyperbolic properties thereby enhancing the radiative heat transfer. Carbon nanotubes, consisting of several rolled-up graphene sheets, showed broadband enhancement in spectral heat flux due to hyperbolic modes along with coupled surface modes[35].

1.5 Objectives of This Current Project

There are several works describing the NFRHT between structures of isotropic materials and layered structures [21],[27–29],[31–34] whereas only few works have been reported in literature describing NFRHT between structures of anisotropic material[26],[30],[35] (only graphite). In this project, the aim is to study NFRHT between Boron Nitride nanotubes (BNNTs), a nanotube structure of hBN. BNNTs are rolled up cylinders consisting of several layers of hBN. They are wide bandgap semiconductors (~6.0 eV) and are transparent in visible spectrum[36]. Fabrication of these high quality BNNTs was performed by ref. [37] via induction thermal plasma process and by ref.[38]

via pressurized vapor/condenser method. Different techniques on fabrication of BNNTs is presented in this review work[36].

So, the current work studies the control of hyperbolic behavior using BNNTs thin films and its impact on NFRHT. Optical properties of BNNTs are calculated by homogenizing the inhomogeneous nanotube structure via Maxwell-Garnet effective medium theory and its corresponding hyperbolic modes are identified. The calculated optical properties coupled with anisotropic thin film optics is used to calculate NFRHT. Investigations on control of hyperbolic band and its impact on NFRHT is studied by varying the volumetric filling ratio and thickness of BNNTs film. Enhancement in near-field radiation due to possible modes is also investigated. In the end, Effectiveness of the control is assessed by calculating spectral allocation ratio which is defined as the total heat flux contributed from the higher frequencies to that of lower frequencies.

2 SCHEMATIC AND OPTICAL PROPERTIES

2.1 Schematic of NFRHT Between BNNTS and hBN Thin Films

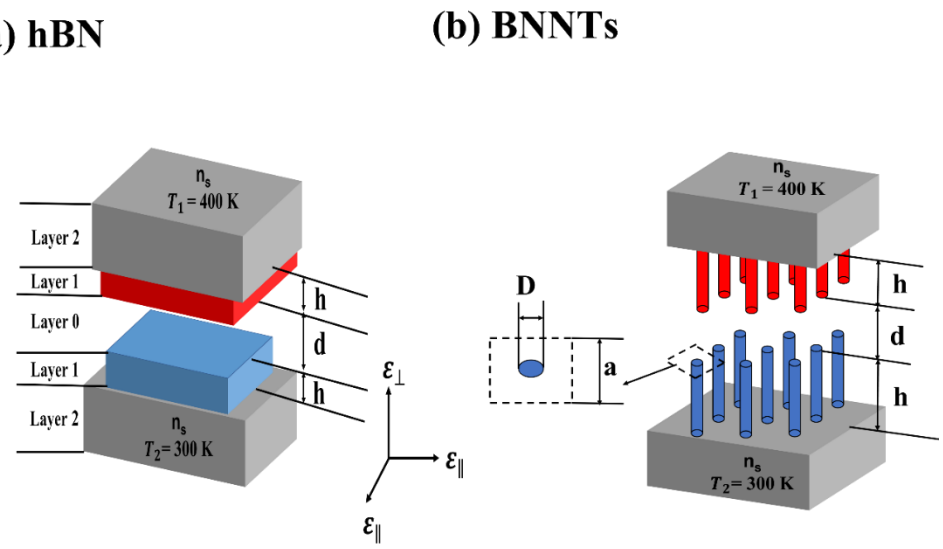

Figure 2.1 Schematic of Near-Field Thermal Radiation for (a) hBN (b) BNNTs

Figure 2.1 (a) and (b) shows the schematic of emitter and receiver configuration with height h, separated by a vacuum gap distance d, for hBN and BNNTs respectively. The temperature of emitter and receiver is assumed to be $T_1 = 400\,K$ and $T_2 = 300\,K$ throughout the current study. Both emitter and receiver films are also assumed to be on top of the same substrate with refractive index n_s and no losses. The direction of component of the dielectric function is defined with respect to the interface of material.

2.2 Optical Properties of hBN

These components, for different frequencies are given by Lorentz model as[21],

$$\varepsilon_l = \varepsilon_{\infty,l}\left[1 + \frac{{\omega_{LO,l}}^2 - {\omega_{TO,l}}^2}{{\omega_{TO,l}}^2 - \omega^2 + j\omega\Gamma_l}\right] \tag{2-1}$$

where l present in subscript of the above equation can either be ∥ or ⊥, ω is angular frequency, Γ is scattering coefficient, ω_{LO} and ω_{TO} are the frequencies of longitudinal and transverse optical phonon modes. The values of ω_{LO}, ω_{TO} and Γ for both the components are shown in [21],

1. Parameters in Lorentz model.

	⊥ component (rad/s)	∥ component (rad/s)
ω_{TO}	1.47×10^{14}	2.58×10^{14}
ω_{LO}	1.56×10^{14}	3.03×10^{14}
Γ	7.54×10^{11}	9.42×10^{11}

2.3 Optical Properties of BNNTs

Figure 2.1 (b) shows the schematic of inhomogeneous aligned BNNTs array arranged in a periodic manner with each tube having a diameter D and unit cell size a. The inset in Figure 2.1 b) also shows the unit cell based on which filling ratio is defined as $f = \frac{\pi D^2}{4a^2}$. Effective medium theory is used to calculate the optical properties by homogenizing the inhomogeneous BNNTs arrays[39]. However, this technique will hold good only when the wavelength of incident electromagnetic radiation is very much greater than unit cell size a. Structures fabricated in ref.[37] and ref.[38] had tube diameters in the order of 5 nm for which value of unit cell size will be around 20 nm corresponding to f = 0.05. The

shortest wavelength that will be dealt with in this study is 4.7 μm (corresponding to $\omega = 4 \times 10^{14}\ rad/s$). So, it is a reasonable approximation to use effective medium theory to calculate the optical properties of BNNTs arrays.

Effective dielectric function of BNNTs can be calculated based on Maxwell-Garnett's effective medium theory as[39] ,

$$\varepsilon_{eff,\parallel} = \frac{\varepsilon_{\perp}(1+f) + \sqrt{\varepsilon_{\perp}/\varepsilon_{\parallel}}(1-f)}{\varepsilon_{\perp}(1-f) + \sqrt{\varepsilon_{\perp}/\varepsilon_{\parallel}}(1+f)} \tag{2-2}$$

$$\varepsilon_{eff,\perp} = f\varepsilon_{\parallel} + (1-f) \tag{2-3}$$

where $\varepsilon_{||}$ and $\varepsilon_{\perp}$ are parallel and perpendicular dielectric function components of hBN respectively.

2.4 Results of Optical Properties

Figure 2.2 (a) and (b) shows the real part of dielectric function for parallel and perpendicular components respectively of both hBN and BNNTs. Figure 2.2 (a) is zoomed in to highlight the positive values of real part of the dielectric function of BNNTs for parallel component. It is seen that hBN has two hyperbolic bands, type I in the frequency band 1.47 × 10^{14} rad/s to 1.56 × 10^{14} rad/s and type II in the frequency band 2.58 × 10^{14} rad/s to 3.03 × 10^{14} rad/s. For BNNTs, there is only one hyperbolic band (type I) observed in higher frequencies for every filling ratio. The main reason for type I hyperbolic band to exist in higher frequency band is due to the shift in transverse and longitudinal optical phonon modes from lower to higher frequencies in the perpendicular component of

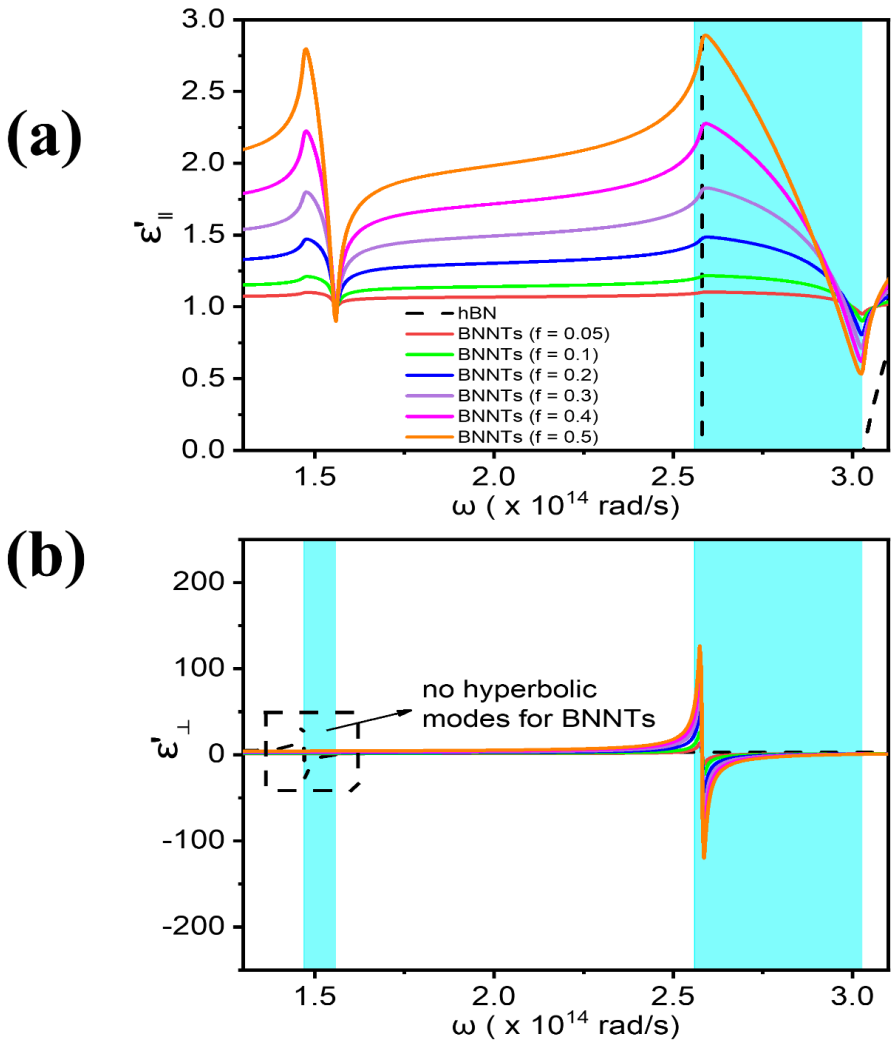

Figure 2.2 Shows the Optical Properties of hBN and BNNTs (a) Parallel Component and (b) Perpendicular Component

dielectric function. There are no hyperbolic bands in lower frequencies because transverse and optical phonon modes vanish in the parallel component of dielectric function. Note: the frequency band in highlighted in Figure 2.2 (a) and (b) are the hyperbolic bands of hBN. However, there is a variation in width of type I hyperbolic band for BNNTs for different filling ratios. The hyperbolic band of BNNTs for different filling ratio is deduced

as follows: f = 0.05-2.58 × 10^{14} rad/s to 2.68 × 10^{14} rad/s; f = 0.1- 2.58 × 10^{14} rad/s to 2.74 × 10^{14} rad/s; f = 0.2-2.58 × 10^{14} rad/s to 2.83 × 10^{14} rad/s; f = 0.3-2.58 × 10^{14} rad/s to 2.89 × 10^{14} rad/s; f = 0.4-2.58 × 10^{14} rad/s to 2.93 × 10^{14} rad/s; f = 0.5-2.58 × 10^{14} rad/s to 2.96 × 10^{14} rad/s. It is clearly seen from the values that width of type I hyperbolic band in BNNTs is increased as the filling ratio is increased.

3 THEORETICAL FORMULATION AND VALIDATION

3.1 NFRHT Formulation Using 4×4 Transfer Matrix Method

The Near-Field Radiative Heat Flux between two anisotropic media based on Fluctuation-Dissipation theorem and reciprocity of Dyadic green function, is given as follows:

$$q = \frac{1}{8\pi^3}\int_0^\infty \Theta(\omega, T_1) - \Theta(\omega, T_2) d\omega \int_0^\infty \int_0^{2\pi} \xi(\omega, \beta, \emptyset)\beta d\beta d\emptyset \tag{3-1}$$

Where $\Theta(\omega, T) = \frac{\hbar\boldsymbol{\omega}}{\exp\left(\frac{\hbar\boldsymbol{\omega}}{k_b T}\right)-1}$, β is parallel wavevector component, $\emptyset$ is the azimuthal angle and $\xi(\omega, \beta, \emptyset)$ is the energy transmission coefficient and it is given by,

$$\xi(\omega, \beta, \emptyset) = \begin{cases} \mathbf{Tr}[(I - {R_2}^* R_2 - {T_2}^* T_2) D (I - {R_1}^* R_1 - {T_1}^* T_1) D^*] & \beta < k_0 \\ \mathbf{Tr}[({R_2}^* - R_2) D ({R_1}^* - R_1) D^*] e^{-2|k_z|d} & \beta > k_0 \end{cases} \tag{3-2}$$

$k_0 = \frac{\omega}{c_0}$ is wavevector in vacuum, $k_z = \sqrt{{k_0}^2 - \beta^2}$ is the perpendicular wavevector component in vacuum, * represents the conjugate transpose of the matrix, $D = \left(I - R_1 R_2 e^{-2jk_z d}\right)^{-1}$, where I is the 2×2 identity matrix and **Tr** represents the trace of the matrix. The Reflection and transmission matrices are given by

$$R_{1,2} = \begin{bmatrix} {r_{ss}}^{1,2} & {r_{sp}}^{1,2} \\ {r_{ps}}^{1,2} & {r_{pp}}^{1,2} \end{bmatrix} \quad T_{1,2} = \begin{bmatrix} {t_{ss}}^{1,2} & {t_{sp}}^{1,2} \\ {t_{ps}}^{1,2} & {t_{pp}}^{1,2} \end{bmatrix} \tag{3-3}$$

The first letter in the subscript of matrix elements indicate the polarization of incident wave and the second letter indicate the polarization reflected or transmitted wave respectively. The cross-polarization terms are zero when the optical axis is perpendicular

to the surface of the material. The elements in the matrix shown in equation (3-3) can be calculated using 4×4 transfer matrix method. This method involves balancing tangential components of electric field and magnetic field at every interface for each ω and β and calculating the elements in equation (3-3). More details of this method are available in ref. [21]

3.2 Preliminary Comparisons with Literature Using 4×4 transfer Matrix Method

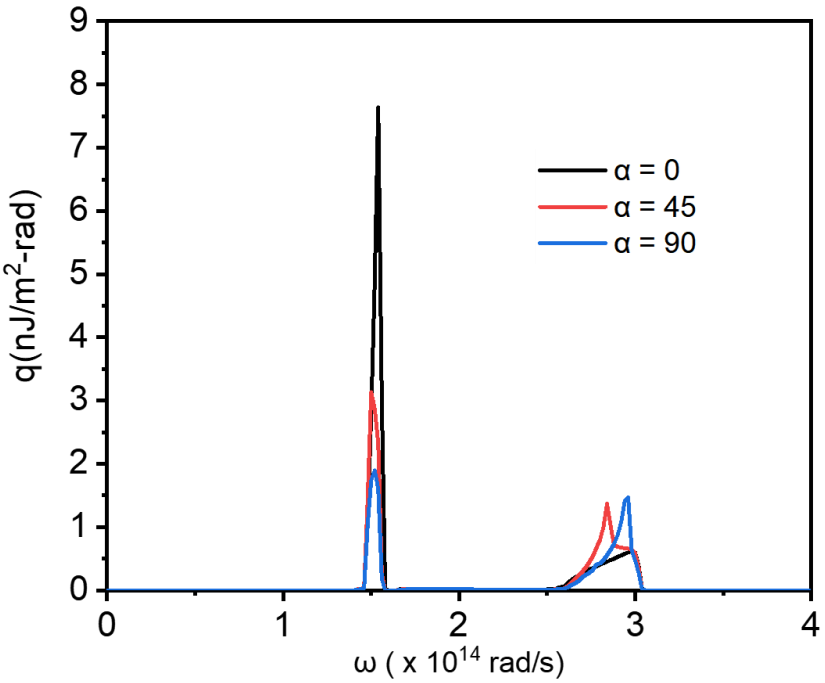

Figure 3.1 Preliminary Comparison of NFRHT Calculations Using 4×4 Transfer Matrix Method with [21] for Different Optical Axis Orientation

Figure 3.1 shows preliminary comparisons of current calculations of NFRHT with [21] for different optical orientations using a more general 4×4 transfer matrix method. α in Figure 3.1 is the angle formed by optical axis with surface normal. The current calculations appear to be matching well with [21] except for the peak around 1.5×10^{14}rad/s where the value of current calculations is slightly lesser than the one

obtained in [21]. The time that was taken to calculate each curve in Figure 3.1 was approximately 1 to 2 hours. Due to high computational time involved, the current project is restricted to the case when optical axis is perpendicular to the surface of the material. For this case, equation (3-1) and (3-2) reduces to a much more simplified form for a 5-layer emitter/substrate and receiver/substrate. Details of those equations are shown in section 3.3.

3.3 NFRHT Formulation Using Anisotropic Thin Film Optics

Anisotropic thin film optics is used to calculate NFRHT when the optical axis is perpendicular to the surface of material. Energy transmission coefficient in equation (3-2) will not depend on azimuthal angle if the optical axis is perpendicular to the surface of the material. So, equation (3-2) reduces to,

$$q = \frac{1}{4\pi^2}\int_0^\infty [\Theta(\omega,T_1)-\Theta(\omega,T_2)]d\omega \int_0^\infty \beta \sum_{\alpha=s,p} \xi_\alpha(\omega,\beta)\, d\beta \tag{3-4}$$

where

$$\xi_\alpha(\omega,\beta) = \begin{cases} \dfrac{\left(1-\left|R_1^{\alpha 2}\right|-\left|T_1^{\alpha 2}\right|\right)^2}{\left|1-R_1^{\alpha 2}e^{i2k_{z0}d}\right|^2}, & \beta < k_0 = \dfrac{\omega}{c} \\ \dfrac{4[Im(R_1^\alpha)]^2 e^{-2Im(k_{z0})d}}{\left|1-R_1^{\alpha 2}e^{i2k_{z0}d}\right|^2}, & \beta > k_0 = \dfrac{\omega}{c} \end{cases} \tag{3-5}$$

$$R_1^\alpha = \frac{r_{01}^\alpha + r_{12}^\alpha e^{i2k_{z1}h_1}}{1+r_{01}^\alpha r_{12}^\alpha e^{i2k_{z1}h_1}} \text{ and } T_1^\alpha = \frac{t_{01}^\alpha t_{12}^\alpha e^{i2k_{z1}h_1}}{1+r_{01}^\alpha r_{12}^\alpha e^{i2k_{z1}h_1}} \tag{3-6}$$

The superscript α indicates the polarization and h_1 is the thickness of layer of material. The Fresnel reflection and transmission coefficients for s and p-polarized waves are given by,

$$r_{j-1,j}^{s} = \frac{k_{z(j-1)}^{s} - k_{zj}^{s}}{k_{z(j-1)}^{s} + k_{zj}^{s}}, r_{j-1,j}^{p} = \frac{\varepsilon_{j,\|} k_{z(j-1)}^{p} - \varepsilon_{j-1,\|} k_{zj}^{p}}{\varepsilon_{j,\|} k_{z(j-1)}^{p} + \varepsilon_{j-1,\|} k_{zj}^{p}} \quad (3\text{-}7)$$

$$t_{j-1,j}^{s} = \frac{2k_{z(j-1)}^{s}}{k_{z(j-1)}^{s} + k_{zj}^{s}}, t_{j-1,j}^{p} = \frac{2\varepsilon_{j,||} k_{z(j-1)}^{p}}{\varepsilon_{j,||} k_{z(j-1)}^{p} + \varepsilon_{j-1,||} k_{zj}^{p}} \quad (3\text{-}8)$$

The subscript j = 0,1,2 in equation (3-7) and (3-8) indicates vacuum, layer of the material and substrate layers respectively. The perpendicular component of wavevectors of s and p polarization for j[th] layer is given by

$$k_{zj}^{s} = \sqrt{\varepsilon_{j,||} {k_o}^2 - \beta^2}, k_{zj}^{p} = \sqrt{\varepsilon_{j,||} {k_o}^2 - \frac{\varepsilon_{j,||}}{\varepsilon_{j,\perp}} \beta^2} \quad (3\text{-}9)$$

For the substrate layer, $k_{z2}^{s} = k_{z2}^{p} = \sqrt{(n_s k_o)^2 - \beta^2}$ and for vacuum, $k_{z0}^{s} = k_{z0}^{p} = \sqrt{{k_o}^2 - \beta^2}$ Before calculating the NFRHT between BNNTs, results of current calculations were compared with existing literature works such as ref. [35] and ref. [23] and the comparisons are shown in next section.

3.4 Comparisons with Literature Using Anisotropic Thin Film Optics

The current calculations have been performed for 1000 equally split angular frequency divisions from $5 \times 10^{12}\, rad/s$ to $4 \times 10^{14}\, rad/s$. 800 β points have been chosen so that distance between two β points is $k_0 = \omega/c$. Numerical tests have been

performed by doubling the β_{max} values. The error in calculating total heat flux is limited 0.01 %. Figure 3.2 (a) and (b) shows the comparison of current calculations of spectral heat flux between two thin hBN films with ref. [23]. To do the comparison, the temperatures of emitter and receiver temperatures are fixed as T_1 = 300 K and T_2 = 0 K respectively and the vacuum gap distance is set to 20 nm. At lower frequencies, the current calculations showed a slightly higher peak value for h = 10 nm which can be accounted by the difference in numerical accuracy of the current calculations and ref. [23]. The rest of the calculations are matching well with ref. [23]. Figure 3.2 (c) shows the comparison of current calculations of spectral heat flux between carbon nanotubes and graphite with the calculations performed by ref. [35].The vacuum gap distance is set to 10 nm and the

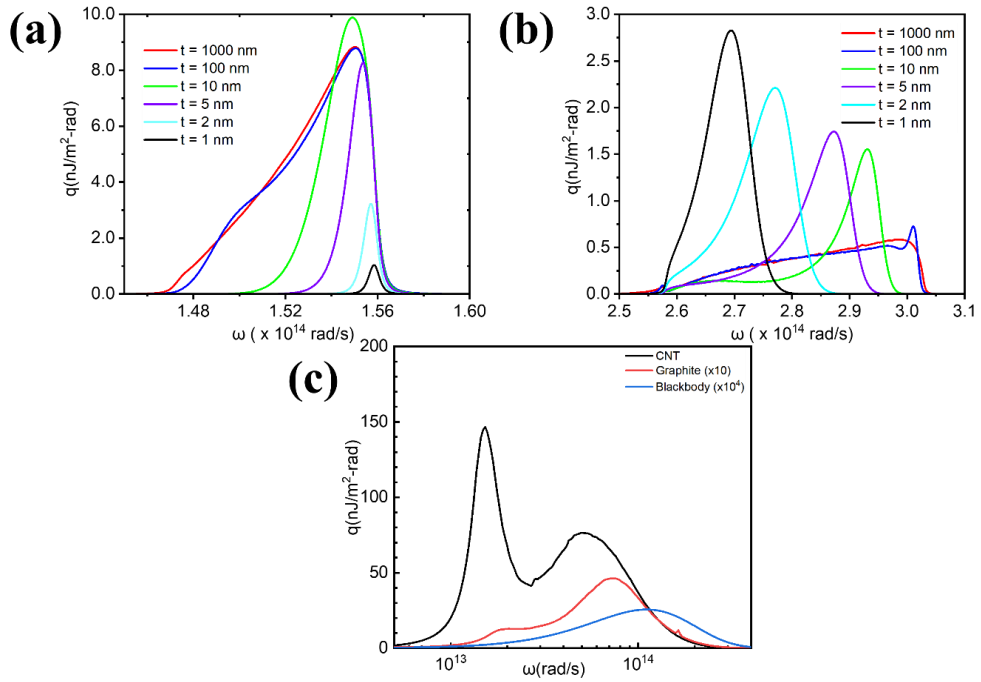

Figure 3.2 Comparison of Current Calculations with Ref. [23] for Thin hBN Sheets (a), (b) and with Ref. [35] Carbon Nanotubes (c)

temperatures remain the same as the previous case. It is observed from Figure 3.2 (c) that the current calculations match the calculations of ref. [35].

4 RESULTS AND DISCUSSIONS

4.1 Spectral Heat Flux

The spectral heat flux is plotted by fixing the gap distance d = 50 nm and substrate as Silicon with $n_s = 3.5$. Figure 4.1 shows the spectral heat flux of BNNTs for different heights h = 25 nm, 50 nm, 100 nm and bulk material and is compared against hBN at various filling ratios. It is clear from Figure 4.1 that there are no peaks in spectral heat flux at lower frequencies for BNNTs due to the absence of hyperbolic bands. But at higher frequencies, peak in spectral heat flux values is higher than hBN for all the heights. For h = 25 nm, at low filling ratios, peak in spectral heat flux is observed around 2.6×10^{14} rad/s. With increase in filling ratios, peak in spectral heat flux shifts to higher frequencies. Let the name of this peak be P-I. For h = 50 nm, new peak (P-II) is observed at higher frequencies for filling ratios $f \geq 0.1$ and with reduction in P-I. For h = 100 nm, there is a further reduction in P-I and increase in P-II such that new peak is greater than the old peak. For infinitely long BNNTs, P-I completely disappears and only P-II is seen. It is also noted from Figure 4.1 that, with increase in height, narrow-banded enhancement in spectral heat flux becomes broad-banded and peak in spectral heat flux value is highest for $f = 0.5$ for infinitely long BNNTs. More results on spectral heat flux with vacuum as a substrate ($n_s = 1$) is shown in APPENDIX A (Figure 1).

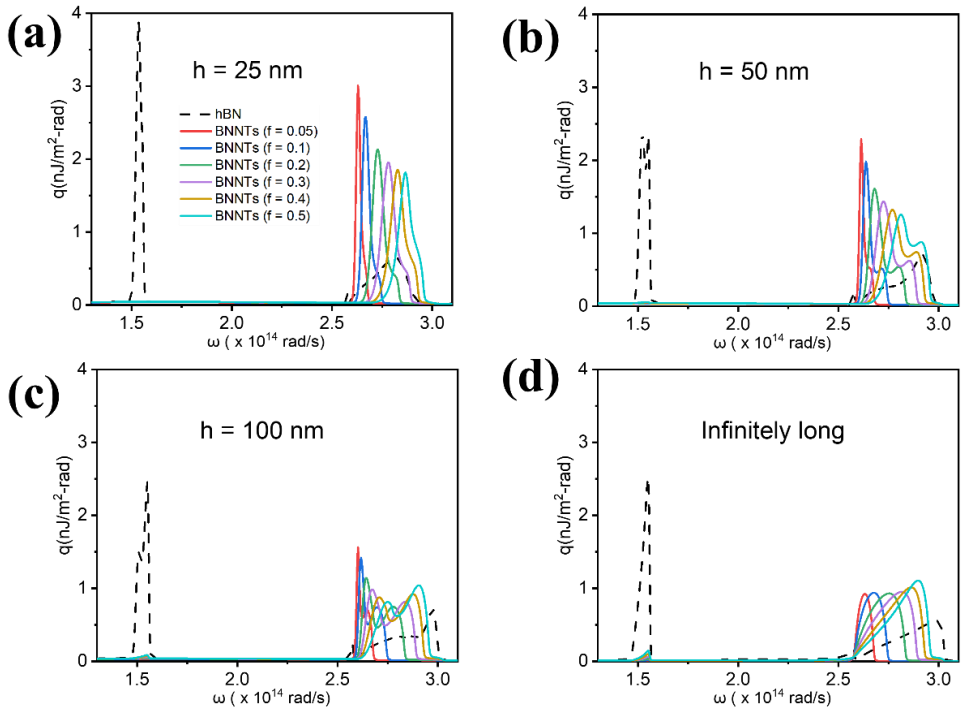

Figure 4.1 Spectral Heat Flux for hBN and BNNTs for d = 50 nm and n_s = 3.5: (a) h = 25 nm (b) h = 50 nm (c) h = 100 nm and (d) Infinitely Long

4.2 Energy Transmission Coefficient

The mechanism of spectral heat flux can be better understood by plotting energy transmission coefficient $\xi(\omega, \beta)$ in the $\omega - \beta$ plane. Figure 4.2 shows the contour plots of energy transmission coefficient for p-polarized waves for BNNTs with heights h = 25 nm, 50 nm, 100 nm and bulk material, by fixing f = 0.5, d = 50 nm and $n_s = 3.5$ in the frequency range 2.6 × 10^{14} rad/s to 3.1 × 10^{14} rad/s. Contribution from p-polarized waves is only plotted since the contribution of s- polarized waves are negligible. It is seen from Figure 4.2 that at lower heights, the enhancement is narrow-banded occupying higher β values. With increase in height, enhancement becomes broad-banded with slight decrease in

maximum β value occupied. This explains the change in narrow-banded enhancement to broad-banded enhancement with increase in height. The split in modes observed at low β values can be explained by plotting the energy transmission coefficient with $n_s = 1$. The plots are shown in APPENDIX B(Figure 2). It is observed that there are no splits in that region when vacuum is used as substrate. This indicates the effects of substrate due to which there is shift in modes of BNNTs. Energy transmission coefficient of hBN for both $n_s = 3.5$ and $n_s = 1$ is shown in APPENDIX C (Figure 3 and Figure 4). Since hBN has a type II hyperbolic band in that frequency range, split in modes occur for $n_s = 1$ and there is no split in modes for $n_s = 3.5$. The physical mechanism for the split in modes can be hypothesized based on the derivation described in APPENDIX D. The derivation equates the denominator of equation (3-7) to zero and obtains the dispersion relation for surface phonon polariton excited at a specfic interface. The obtained dispersion is a circle with radius that depends on the optical properties. After the derivation, for $\omega = 2.9 \times 10^{14}(rad/s)$, the square of radius of the circle is calculated for hBN and BNNTs with $n_s = 3.5$ and $n_s = 1$ respectively. It was observed that for BNNTs with $n_s = 3.5$,the square of radius is negative indicating there is no solution. Due to this, surface phonon polaritons will not be excited at that interface. Based on this, it is hypothesized that there is irregular split in modes due to the absence of surface phonon polaritons at BNNTs/substrate ($n_s = 3.5$) interface.

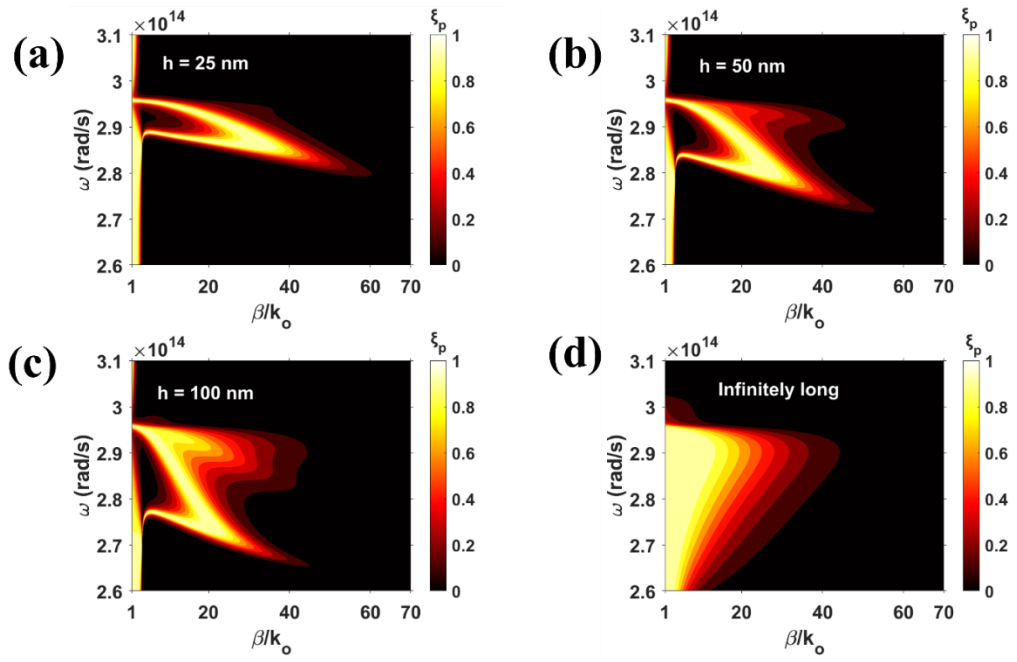

Figure 4.2 Energy Transmission Coefficient of BNNTs with Different Heights for d = 50 nm, f = 0.5 and n_s=3.5: (a) h = 25 nm (b) h = 50 nm (c) h = 100 nm and (d) Infinitely long

4.3 Spectral Allocation Ratio

Instead of plotting total heat flux, spectral allocation ratio $\psi = \frac{q_{higher}}{q_{lower}}$ is plotted for different heights, filling ratios and gap distances is plotted, and it is shown in Figure 4.3. In ψ, q_{higher} is heat flux contribution from the higher frequency band 2.5 × 10^{14} rad/s to 3.1 × 10^{14} rad/s and q_{lower} is the heat flux contribution from the lower frequency band 1.4 × 10^{14} rad/s to 1.6 × 10^{14} rad/s. Beyond 200 nm, there is no subtle difference in the values for different filling ratios and hence is not shown here. It is seen that spectral allocation ratio for hBN is almost close to 1 for lower gap distances and it decreases even further with increase in gap distance. For BNNTs, ψ increases up to f = 0.3 and it decreases if the filling ratio is further increased. However, the decrease is not significant. Also, it is interesting to note that ψ can reach as high as 55 for infinitely long BNNTs with filling ratio f = 0.3. ψ

is less for smaller heights for a given filling ratio and it increases with increase in height indicating that lower frequency contribution diminishes with increase in height. More results of spectral allocation ratio with vacuum as a substrate is shown in APPENDIX E, Figure 5.

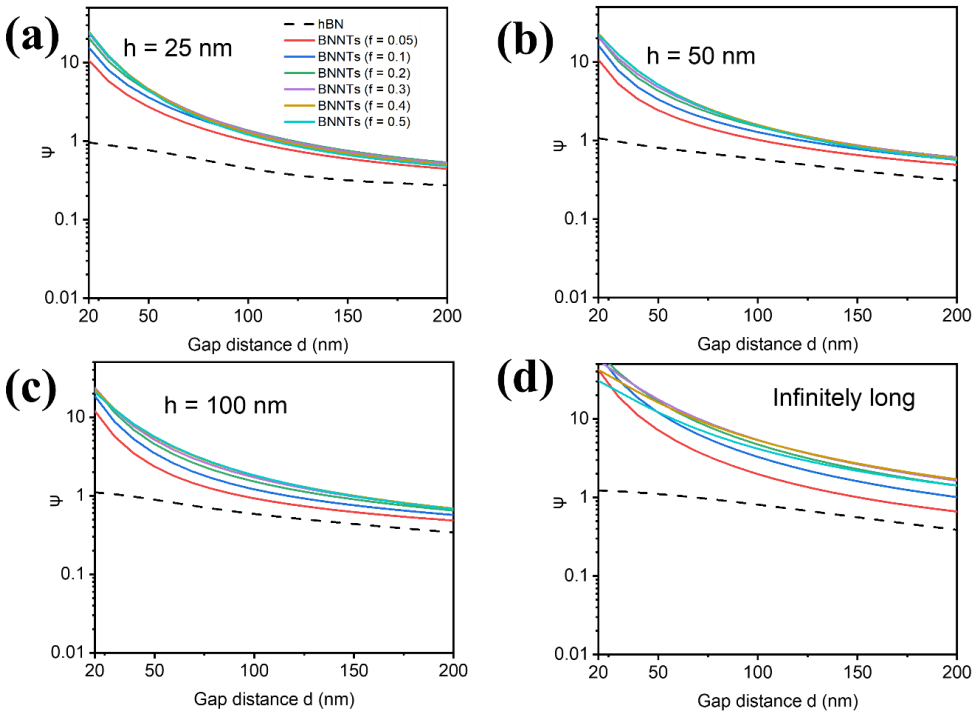

Figure 4.3 Spectral Allocation Ratio for hBN and BNNTs for n_s=3.5: a) h = 25 nm b) h = 50 nm c) h = 100 nm and d) Bulk

5 CONCLUSIONS AND FUTURE WORKS

The control of hyperbolic behavior using BNNTs for NFRHT is investigated. Optical properties of BNNTs are calculated based on Maxwell-Garnett's effective theory. The control is achieved by switching off the hyperbolic band in lower frequencies and changing the hyperbolic band to type I. The main reason for this control is due to the shift in transverse and longitudinal optical phonon modes from lower to higher frequencies in the perpendicular component of dielectric function. With this control, it is possible to tune the frequencies at which hyperbolic modes are excited. By changing the filling ratio of BNNTs, width of the hyperbolic bands is also controlled. These two controls can have significant impact on NFRHT.

Spectral heat flux for BNNTs showed no peaks at lower frequencies due to the absence of hyperbolic bands. Also, peak in spectral heat flux is highest for f = 0.05 when the thickness is h = 25 nm. With increase in thickness, new peaks appear when filling ratio is $f \geq 0.1$. The new peak is highest for $f = 0.5$ and is less than old peak for h = 50 nm. For h = 100 nm, new peak is higher than the old peak. For the infinitely long case, there is a broadband enhancement in spectral heat flux.

Plotting the energy transmission coefficient, delineated the some of the trends observed in spectral heat flux. The physical mechanism for the observed transmission coefficient is hypothesized based on the dispersion relation of surface phonon polariton excited at the interface. It was observed that surface phonon polariton was not excited at

the interface of BNNTs/substrate ($n_s = 3.5$) due to which there is irregular split in modes for BNNTs when $n_s = 3.5$

It is also observed that spectral allocation ratio is higher for BNNTs than hBN. For cases of BNNTs with smallest height, spectral allocation ratio is the smallest and it increases with increase in height for every gap distance.

In future, a detailed investigations must be performed explaining the physical mechanisms behind the split in modes for BNNTs. Also, near-field experimental measurements must be performed to prove this theoretically proposed control.

REFERENCES

[1] Modest, Michael. F. *Fundamentals of Thermal Radiation*.

[2] Zhang, Z. M. *Mechanical Engineering Series*.

[3] Cuevas, J. C., and García-Vidal, F. J. Radiative Heat Transfer. *ACS Photonics*. 10. Volume 5, 3896–3915.

[4] Chang, J. Y., Yang, Y., and Wang, L. "Tungsten Nanowire Based Hyperbolic Metamaterial Emitters for Near-Field Thermophotovoltaic Applications." *International Journal of Heat and Mass Transfer*, Vol. 87, 2015, pp. 237–247. https://doi.org/10.1016/j.ijheatmasstransfer.2015.03.087.

[5] Messina, R., and Ben-Abdallah, P. "Graphene-Based Photovoltaic Cells for near-Field Thermal Energy Conversion." *Scientific Reports*, Vol. 3, 2013. https://doi.org/10.1038/srep01383.

[6] Vongsoasup, N., Francoeur, M., and Hanamura, K. "Performance Analysis of Near-Field Thermophotovoltaic System with 2D Grating Tungsten Radiator." *International Journal of Heat and Mass Transfer*, Vol. 115, 2017, pp. 326–332. https://doi.org/10.1016/j.ijheatmasstransfer.2017.07.070.

[7] Yu, H., Duan, Y., and Yang, Z. "Selectively Enhanced Near-Field Radiative Transfer between Plasmonic Emitter and GaSb with Nanohole and Nanowire Periodic Arrays for Thermophotovoltaics." *International Journal of Heat and Mass Transfer*, Vol. 123, 2018, pp. 67–74. https://doi.org/10.1016/j.ijheatmasstransfer.2018.02.085.

[8] Guha, B., Otey, C., Poitras, C. B., Fan, S., and Lipson, M. "Near-Field Radiative Cooling of Nanostructures." *Nano Letters*, Vol. 12, No. 9, 2012, pp. 4546–4550. https://doi.org/10.1021/nl301708e.

[9] Chen, K., Santhanam, P., and Fan, S. "Near-Field Enhanced Negative Luminescent Refrigeration." *Physical Review Applied*, Vol. 6, No. 2, 2016. https://doi.org/10.1103/PhysRevApplied.6.024014.

[10] Ben-Abdallah, P., and Biehs, S. A. "Near-Field Thermal Transistor." *Physical Review Letters*, Vol. 112, No. 4, 2014. https://doi.org/10.1103/PhysRevLett.112.044301.

[11] Gu, W., Tang, G. H., and Tao, W. Q. "Thermal Switch and Thermal Rectification Enabled by Near-Field Radiative Heat Transfer between Three Slabs." *International Journal of Heat and Mass Transfer*, Vol. 82, 2015, pp. 429–434. https://doi.org/10.1016/j.ijheatmasstransfer.2014.11.058.

[12] Otey, C. R., Lau, W. T., and Fan, S. "Thermal Rectification through Vacuum." *Physical Review Letters*, Vol. 104, No. 15, 2010. https://doi.org/10.1103/PhysRevLett.104.154301.

[13] Francoeur, M., Mengüç, M. P., and Vaillon, R. "Coexistence of Multiple Regimes for Near-Field Thermal Radiation between Two Layers Supporting Surface Phonon Polaritons in the Infrared." *Physical Review B - Condensed Matter and Materials Physics*, Vol. 84, No. 7, 2011. https://doi.org/10.1103/PhysRevB.84.075436.

[14] Francoeur, M., Mengü, M. P., and Vaillon, R. "Near-Field Radiative Heat Transfer Enhancement via Surface Phonon Polaritons Coupling in Thin Films." *Applied Physics Letters*, Vol. 93, No. 4, 2008. https://doi.org/10.1063/1.2963195.

[15] Lee, B. J., and Zhang, Z. M. "Lateral Shifts in Near-Field Thermal Radiation with Surface Phonon Polaritons." *Nanoscale and Microscale Thermophysical Engineering*, Vol. 12, No. 3, 2008, pp. 238–250. https://doi.org/10.1080/15567260802247505.

[16] Francoeur, M., Mengü, M. P., and Vaillon, R. "Local Density of Electromagnetic States within a Nanometric Gap Formed between Two Thin Films Supporting Surface Phonon Polaritons." *Journal of Applied Physics*, Vol. 107, No. 3, 2010. https://doi.org/10.1063/1.3294606.

[17] Ghashami, M., Geng, H., Kim, T., Iacopino, N., Cho, S. K., and Park, K. "Precision Measurement of Phonon-Polaritonic Near-Field Energy Transfer between Macroscale Planar Structures under Large Thermal Gradients." *Physical Review Letters*, Vol. 120, No. 17, 2018. https://doi.org/10.1103/PhysRevLett.120.175901.

[18] Lim, M., Lee, S. S., and Lee, B. J. "Near-Field Thermal Radiation between Doped Silicon Plates at Nanoscale Gaps." *Physical Review B - Condensed Matter and Materials Physics*, Vol. 91, No. 19, 2015. https://doi.org/10.1103/PhysRevB.91.195136.

[19] Basu, S., Lee, B. J., and Zhang, Z. M. "Near-Field Radiation Calculated with an Improved Dielectric Function Model for Doped Silicon." *Journal of Heat Transfer*, Vol. 132, No. 2, 2010, pp. 1–7. https://doi.org/10.1115/1.4000179.

[20] Francoeur, M., Mengüç, M. P., and Vaillon, R. "Spectral Tuning of Near-Field Radiative Heat Flux between Two Thin Silicon Carbide Films." *Journal of Physics D: Applied Physics*, Vol. 43, No. 7, 2010, p. 075501. https://doi.org/10.1088/0022-3727/43/7/075501.

[21] Wu, X., Fu, C., and Zhang, Z. "Influence of HBN Orientation on the Near-Field Radiative Heat Transfer between Graphene/HBN Heterostructures." *Journal of Photonics for Energy*, Vol. 9, No. 03, 2018, p. 1. https://doi.org/10.1117/1.jpe.9.032702.

[22] Liu, X. L., and Xuan, Y. M. "Super-Planckian Thermal Radiation Enabled by Hyperbolic Surface Phonon Polaritons." *Science China Technological Sciences*, Vol. 59, No. 11, 2016, pp. 1680–1686. https://doi.org/10.1007/s11431-016-0480-9.

[23] Wu, X., and Fu, C. "Near-Field Radiative Heat Transfer between Uniaxial Hyperbolic Media: Role of Volume and Surface Phonon Polaritons." *Journal of*

Quantitative Spectroscopy and Radiative Transfer, Vol. 258, 2021. https://doi.org/10.1016/j.jqsrt.2020.107337.

[24] Salihoglu, H., and Xu, X. "Near-Field Radiative Heat Transfer Enhancement Using Natural Hyperbolic Material." *Journal of Quantitative Spectroscopy and Radiative Transfer*, Vols. 222–223, 2019, pp. 115–121. https://doi.org/10.1016/j.jqsrt.2018.10.022.

[25] Wu, X., Fu, C., and Zhang, Z. M. "Near-Field Radiative Heat Transfer between Two α-MoO3biaxial Crystals." *Journal of Heat Transfer*, Vol. 142, No. 7, 2020. https://doi.org/10.1115/1.4046968.

[26] Zhang, R. Z., Liu, X., and Zhang, Z. M. "Near-Field Radiation between Graphene-Covered Carbon Nanotube Arrays." *AIP Advances*, Vol. 5, No. 5, 2015. https://doi.org/10.1063/1.4913993.

[27] Shi, K., Bao, F., and He, S. "Enhanced Near-Field Thermal Radiation Based on Multilayer Graphene-HBN Heterostructures." *ACS Photonics*, Vol. 4, No. 4, 2017, pp. 971–978. https://doi.org/10.1021/acsphotonics.7b00037.

[28] Wu, X., and Liu, R. "Near-Field Radiative Heat Transfer between Graphene Covered Biaxial Hyperbolic Materials." *ES Energy & Environment*, 2020. https://doi.org/10.30919/esee8c939.

[29] Liu, X. L., Zhang, R. Z., and Zhang, Z. M. "Near-Field Radiative Heat Transfer with Doped-Silicon Nanostructured Metamaterials." *International Journal of Heat and Mass Transfer*, Vol. 73, 2014, pp. 389–398. https://doi.org/10.1016/j.ijheatmasstransfer.2014.02.021.

[30] Shen, J., Liu, X., and Xuan, Y. "Near-Field Thermal Radiation between Nanostructures of Natural Anisotropic Material." *Physical Review Applied*, Vol. 10, No. 3, 2018. https://doi.org/10.1103/PhysRevApplied.10.034029.

[31] Guo, Y., Cortes, C. L., Molesky, S., and Jacob, Z. "Broadband Super-Planckian Thermal Emission from Hyperbolic Metamaterials." *Applied Physics Letters*, Vol. 101, No. 13, 2012. https://doi.org/10.1063/1.4754616.

[32] Biehs, S. A., Tschikin, M., Messina, R., and Ben-Abdallah, P. "Super-Planckian near-Field Thermal Emission with Phonon-Polaritonic Hyperbolic Metamaterials." *Applied Physics Letters*, Vol. 102, No. 13, 2013. https://doi.org/10.1063/1.4800233.

[33] Basu, S., and Wang, L. "Near-Field Radiative Heat Transfer between Doped Silicon Nanowire Arrays." *Applied Physics Letters*, Vol. 102, No. 5, 2013. https://doi.org/10.1063/1.4790143.

[34] Biehs, S. A., Tschikin, M., and Ben-Abdallah, P. "Hyperbolic Metamaterials as an Analog of a Blackbody in the near Field." *Physical Review Letters*, Vol. 109, No. 10, 2012. https://doi.org/10.1103/PhysRevLett.109.104301.

[35] Liu, X. L., Zhang, R. Z., and Zhang, Z. M. "Near-Field Thermal Radiation between Hyperbolic Metamaterials: Graphite and Carbon Nanotubes." *Applied Physics Letters*, Vol. 103, No. 21, 2013. https://doi.org/10.1063/1.4832057.

[36] Rao, R., Pint, C. L., Islam, A. E., Weatherup, R. S., Hofmann, S., Meshot, E. R., Wu, F., Zhou, C., Dee, N., Amama, P. B., Carpena-Nuñez, J., Shi, W., Plata, D. L., Penev, E. S., Yakobson, B. I., Balbuena, P. B., Bichara, C., Futaba, D. N., Noda, S., Shin, H., Kim, K. S., Simard, B., Mirri, F., Pasquali, M., Fornasiero, F., Kauppinen, E. I., Arnold, M., Cola, B. A., Nikolaev, P., Arepalli, S., Cheng, H. M., Zakharov, D. N., Stach, E. A., Zhang, J., Wei, F., Terrones, M., Geohegan, D. B., Maruyama, B., Maruyama, S., Li, Y., Adams, W. W., and Hart, A. J. Carbon Nanotubes and Related Nanomaterials: Critical Advances and Challenges for Synthesis toward Mainstream Commercial Applications. *ACS Nano*. 12. Volume 12, 11756–11784.

[37] Kim, K. S., Kingston, C. T., Hrdina, A., Jakubinek, M. B., Guan, J., Plunkett, M., and Simard, B. "Hydrogen-Catalyzed, Pilot-Scale Production of Small-Diameter Boron Nitride Nanotubes and Their Macroscopic Assemblies." *ACS Nano*, Vol. 8, No. 6, 2014, pp. 6211–6220. https://doi.org/10.1021/nn501661p.

[38] Smith, M. W., Jordan, K. C., Park, C., Kim, J. W., Lillehei, P. T., Crooks, R., and Harrison, J. S. "Very Long Single-and Few-Walled Boron Nitride Nanotubes via the Pressurized Vapor/Condenser Method." *Nanotechnology*, Vol. 20, No. 50, 2009. https://doi.org/10.1088/0957-4484/20/50/505604.

[39] García-Vidal, F. J., Pitarke, J. M., and Pendry, J. B. *Effective Medium Theory of the Optical Properties of Aligned Carbon Nanotubes*. 1997.

APPENDIX A

SPECTRAL HEAT FLUX WITH $n_s = 1$

The current section plots the spectral heat flux with $n_s = 1$. Figure 1 shows the spectral heat flux of BNNTs for different heights h = 25 nm, 50 nm, 100 nm at various filling ratios. For this case, new peaks are observed for h = 100 nm and enhancement is becoming broadband as heights are increased. Similar to Figure 4.1, to peak in spectral heat flux is pushed to higher frequencies as the filling ratio is increased for a given height. Also, peak for hBN is observed at edge of its type II hyperbolic band and its value is almost same as that of BNNTs with higher filling ratios (peak for hBN is lesser than BNNTs with higher filling ratios for n_s = 3.5).

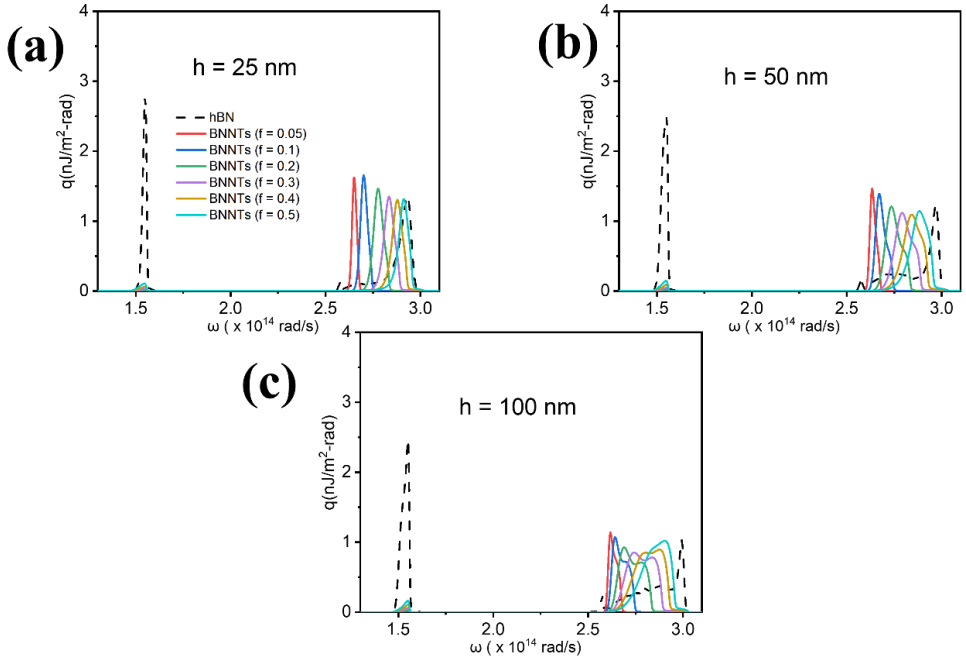

Figure 1 Spectral Heat Flux for hBN and BNNTs for d = 50 nm and n_s=1: (a) h = 25 nm (b) h = 50 nm and (c) h = 100 nm

APPENDIX B

ENERGY TRANSMISSION COEFFICIENT OF BNNTS

Figure 2 shows the energy transmission coefficient for BNNTs for heights h = 25 nm, h = 50 nm and h = 100 nm with substrate $n_s = 1$. It is clear from Figure 2 that there are no split in modes when vacuum is used as substrate. This indicates the substrate play a major role in split of modes. Similar to Figure 4.2, narrow-banded enhancement to broadband enhancment is also observed here.

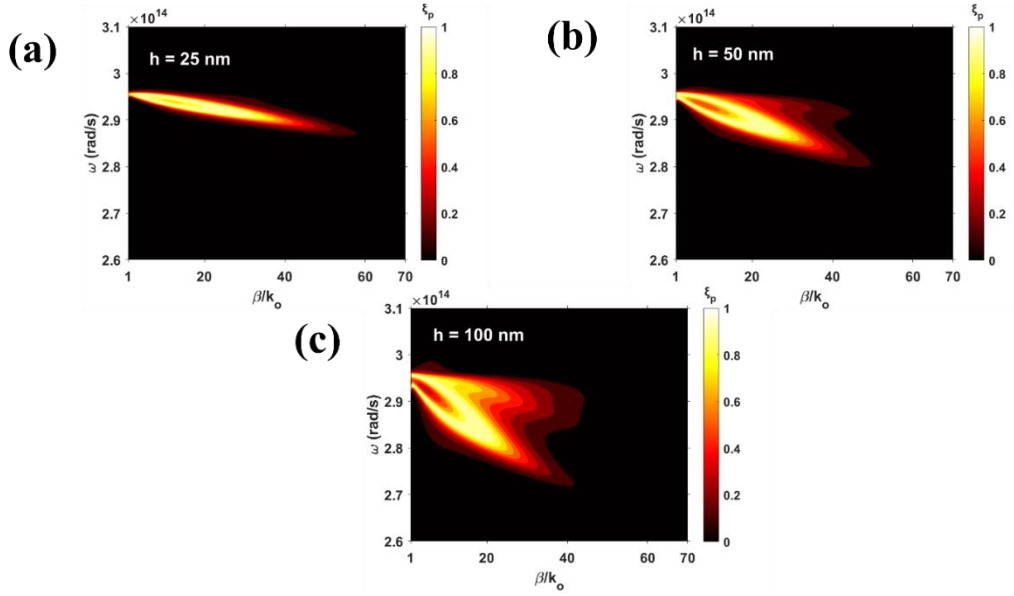

Figure 2 Energy Transmission Coefficient of BNNTs at different heights for d = 50 nm, f = 0.5 and n_s=1: (a) h = 25 nm (b) h = 50 nm and (c) h = 100 nm

APPENDIX C

ENERGY TRANSMISSION COEFFICIENT FOR hBN

Figure 3 shows the energy transmission coefficient for hBN at higher frequencies for heights h = 25 nm, h = 50 nm and h = 100 nm with $n_s = 3.5$. With $n_s = 3.5$, substrate, the split in modes is lesser. When vacuum is used as the substrate, there split in modes is large (Figure 4). This behavior observed for hBN is in contrast with BNNTs. This is because in the frequency range plotted, hBN show type II hyperbolic band whereas BNNTs show type I hyperbolic band.

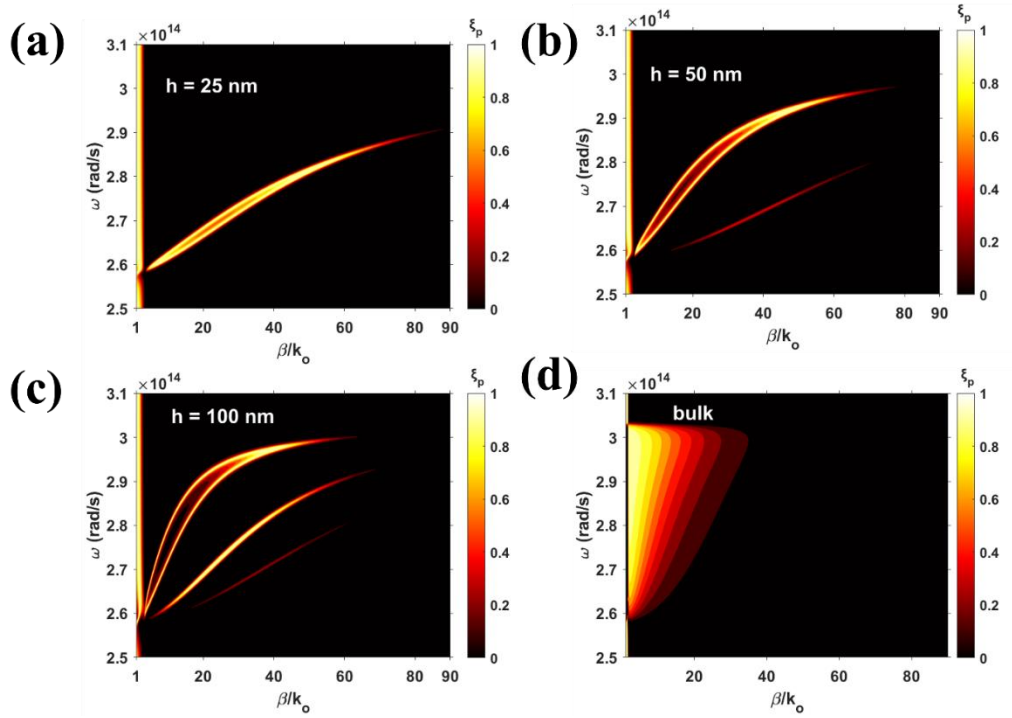

Figure 3 Energy Transmission Coefficient of hBN at Different Heights for d = 50 nm and n_s=3.5: (a) h = 25 nm (b) h = 50 nm (c) h = 100 nm and (d) Bulk

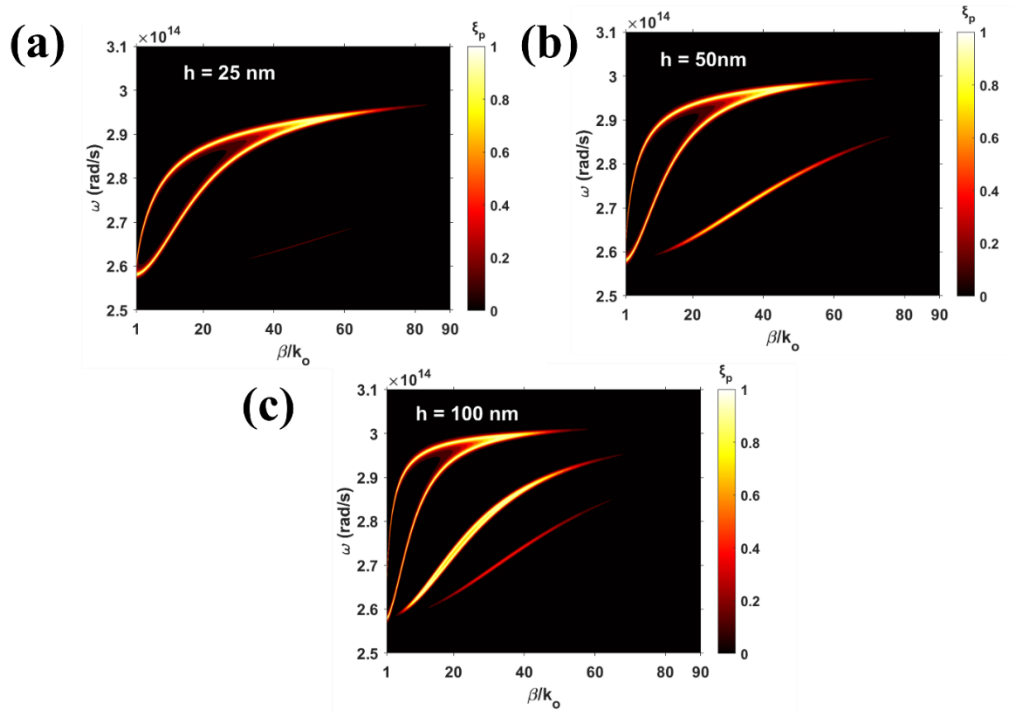

Figure 4 Energy Transmission Coefficient of hBN at Different Heights for d = 50 nm and n_s=1: (a) h = 25 nm (b) h = 50 nm and (c) h = 100 nm

APPENDIX D

DERIVATION OF DISPERSION RELATION

The Fresnel reflection and transmission coefficients at the interface between a uniaxial material and a isotropic material are given by equation (3-7) and (3-8) as,

$$r_{j-1,j}^{p} = \frac{\varepsilon_{j,\parallel} k_{z(j-1)}^{p} - \varepsilon_{j-1,\parallel} k_{zj}^{p}}{\varepsilon_{j,\parallel} k_{z(j-1)}^{p} + \varepsilon_{j-1,\parallel} k_{zj}^{p}}, t_{j-1,j}^{p} = \frac{2\varepsilon_{j,||} k_{z(j-1)}^{p}}{\varepsilon_{j,||} k_{z(j-1)}^{p} + \varepsilon_{j-1,||} k_{zj}^{p}}$$

Zeroing the denominator of above Fresnel coefficients will give dispersion relation of surface phonon polaritons excited at the interface between two media.[21,22]

$$\varepsilon_{j,\parallel} k_{z(j-1)}^{p} + \varepsilon_{j-1,\parallel} k_{zj}^{p} = 0 \quad (1)$$

$$k_{zj}^{p} = \sqrt{\varepsilon_{j,||} {k_o}^2 - \frac{\varepsilon_{j,||}}{\varepsilon_{j,\perp}} \beta^2}, k_{z(j-1)}^{p} = \sqrt{\varepsilon_{j-1,||} {k_o}^2 - \frac{\varepsilon_{j-1,||}}{\varepsilon_{j-1,\perp}} \beta^2} \quad (2)$$

Substituting equation (2) in (1) we get,

$$\varepsilon_{j,\parallel} \sqrt{\varepsilon_{j-1,||} {k_o}^2 - \frac{\varepsilon_{j-1,||}}{\varepsilon_{j-1,\perp}} \beta^2} + \varepsilon_{j-1,\parallel} \sqrt{\varepsilon_{j,||} {k_o}^2 - \frac{\varepsilon_{j,||}}{\varepsilon_{j,\perp}} \beta^2} = 0$$

Rearranging the terms and solving for β^2,

$$\frac{\varepsilon_{j,\parallel}}{\varepsilon_{j-1,\parallel}} = -\frac{\sqrt{\varepsilon_{j,\parallel} {k_o}^2 - \frac{\varepsilon_{j,\parallel}}{\varepsilon_{j,\perp}} \beta^2}}{\sqrt{\varepsilon_{j-1,\parallel} {k_o}^2 - \frac{\varepsilon_{j-1,\parallel}}{\varepsilon_{j-1,\perp}} \beta^2}}$$

$$\left(\frac{\varepsilon_{j,\parallel}}{\varepsilon_{j-1,\parallel}}\right)^2 = \frac{\varepsilon_{j,\parallel} {k_o}^2 - \frac{\varepsilon_{j,\parallel}}{\varepsilon_{j,\perp}} \beta^2}{\varepsilon_{j-1,\parallel} {k_o}^2 - \frac{\varepsilon_{j-1,\parallel}}{\varepsilon_{j-1,\perp}} \beta^2}$$

$$\varepsilon_{j,\|}^2\left(\varepsilon_{j-1,\|}{k_o}^2-\frac{\varepsilon_{j-1,\|}}{\varepsilon_{j-1,\perp}}\beta^2\right)=\ \varepsilon_{j-1,\|}^2\left(\varepsilon_{j,\|}{k_o}^2-\frac{\varepsilon_{j,\|}}{\varepsilon_{j,\perp}}\beta^2\right)$$

$$\beta^2\left(\varepsilon_{j-1,\|}^2\frac{\varepsilon_{j,\|}}{\varepsilon_{j,\perp}}-\ \varepsilon_{j,\|}^2\frac{\varepsilon_{j-1,\|}}{\varepsilon_{j-1,\perp}}\right)=k_o^2\left(\varepsilon_{j-1,\|}^2\varepsilon_{j,\|}-\ \varepsilon_{j,\|}^2\varepsilon_{j-1,\|}\right)$$

$$\beta^2=k_x^2+k_y^2=\frac{k_o^2\left(\varepsilon_{j-1,\|}^2\varepsilon_{j,\|}-\ \varepsilon_{j,\|}^2\varepsilon_{j-1,\|}\right)}{\varepsilon_{j-1,\|}^2\frac{\varepsilon_{j,\|}}{\varepsilon_{j,\perp}}-\ \varepsilon_{j,\|}^2\frac{\varepsilon_{j-1,\|}}{\varepsilon_{j-1,\perp}}}$$

$$\beta^2=k_x^2+k_y^2=\frac{k_o^2\left(\varepsilon_{j-1,\|}^2\varepsilon_{j,\|}-\ \varepsilon_{j,\|}^2\varepsilon_{j-1,\|}\right)}{\varepsilon_{j-1,\|}^2\frac{\varepsilon_{j,\|}}{\varepsilon_{j,\perp}}-\ \varepsilon_{j,\|}^2\frac{\varepsilon_{j-1,\|}}{\varepsilon_{j-1,\perp}}} \tag{3}$$

For vacuum/uniaxial interface (interface 01), $\varepsilon_{0,\|}=\varepsilon_{0,\perp}=\varepsilon_0=1$

So, equation (3) becomes,

$$k_x^2+k_y^2=\frac{k_o^2\left(\varepsilon_0^2\varepsilon_{1,\|}-\ \varepsilon_{1,\|}^2\varepsilon_0\right)}{\varepsilon_0^2\frac{\varepsilon_{1,\|}}{\varepsilon_{1,\perp}}-\ \varepsilon_{1,\|}^2}=a_o^2$$

$$k_x^2+k_y^2=\frac{k_o^2\left(\varepsilon_0^2\varepsilon_{1,\|}\varepsilon_{1,\perp}-\ \varepsilon_{1,\|}^2\varepsilon_{1,\perp}\varepsilon_0\right)}{\varepsilon_0^2\varepsilon_{1,\|}-\ \varepsilon_{1,\|}^2\varepsilon_{1,\perp}}=a_o^2$$

$$k_x^2+k_y^2=\frac{k_o^2\left(\varepsilon_0^2\varepsilon_{1,\|}\varepsilon_{1,\perp}-\ \varepsilon_{1,\|}^2\varepsilon_{1,\perp}\varepsilon_0\right)}{\varepsilon_0^2\varepsilon_{1,\|}-\ \varepsilon_{1,\|}^2\varepsilon_{1,\perp}}=a_o^2 \tag{0-1}$$

For uniaxial/substrate interface (interface 12), $\varepsilon_{2,\|}=\varepsilon_{2,\perp}=\varepsilon_s$. This will modify equation (3) as,

$$k_x^2 + k_y^2 = \frac{k_o^2\left(\varepsilon_{1,\parallel}^2\varepsilon_s - \varepsilon_s^2\varepsilon_{1,\parallel}\right)}{\varepsilon_{1,\parallel}^2 - \varepsilon_s^2\frac{\varepsilon_{1,\parallel}}{\varepsilon_{1,\perp}}}$$

$$k_x^2 + k_y^2 = \frac{k_o^2\left(\varepsilon_{1,\parallel}^2\varepsilon_{1,\perp}\varepsilon_s - \varepsilon_s^2\varepsilon_{1,\perp}\varepsilon_{1,\parallel}\right)}{\varepsilon_{1,\parallel}^2\varepsilon_{1,\perp} - \varepsilon_s^2\varepsilon_{1,\parallel}} = a_s^2$$

$$k_x^2 + k_y^2 = \frac{k_o^2\left(\varepsilon_{1,\parallel}^2\varepsilon_{1,\perp}\varepsilon_s - \varepsilon_s^2\varepsilon_{1,\perp}\varepsilon_{1,\parallel}\right)}{\varepsilon_{1,\parallel}^2\varepsilon_{1,\perp} - \varepsilon_s^2\varepsilon_{1,\parallel}} = a_s^2 \qquad (0\text{-}2)$$

The right-hand side of equation (0-1) and (0-2) are calculated for both hBN and BNNTs. The values are calculated with only real parts of the dielectric function.

hBN:

For $\omega = 2.9 \times 10^{14} rad/s$, $\varepsilon_{1,\parallel} = -2.139 + 0.109i, \varepsilon_{1,\perp} = 2.821 + 0.0004i$

For vacuum substrate: $a_0^2 = 1.17 \times 10^{12}$

For Silicon substrate (n_s = 3.5): $a_s^2 = 2.97 \times 10^{12}$

BNNTs:

For $\omega = 2.9 \times 10^{14} rad/s$, $\varepsilon_{1,\parallel} = 1.411 + 1.275i, \varepsilon_{1,\perp} = -0.569 + 0.054i$

For vacuum substrate: $a_0^2 = 1.21 \times 10^{11}$

For Silicon substrate (n_s = 3.5): $a_s^2 = -4.68 \times 10^{11}$

From the above calculations, it can be inferred that no solution exists for equation (0-2) around $2.9 \times 10^{14} rad/s$ since a_s^2 is negative. This indicates that surface phonon polaritons will not be excited at BNNTs/substrate ($n_s = 3.5$) interface.

APPENDIX E

SPECTRAL ALLOCATION RATIO FOR n_S= 1:

Figure 5 shows the spectral allocation ratio when $n_s = 1$. For each thickness chosen, there is a subtle difference in spectral allocation ratio among each filling ratio whereas for $n_s = 3.5$ spectral allocation ratio almost fall on top of each other (Figure 4.3). The maximum spectral allocation ratio achieved is around 787 for the parameters f = 0.05, d = 20nm and h = 25 nm which is higher than the maximum value when $n_s = 3.5$ is used as a substrate (around 55). It also decreases with increase in filling ratio, and it is the lowest for f = 0.5 among BNNTs.

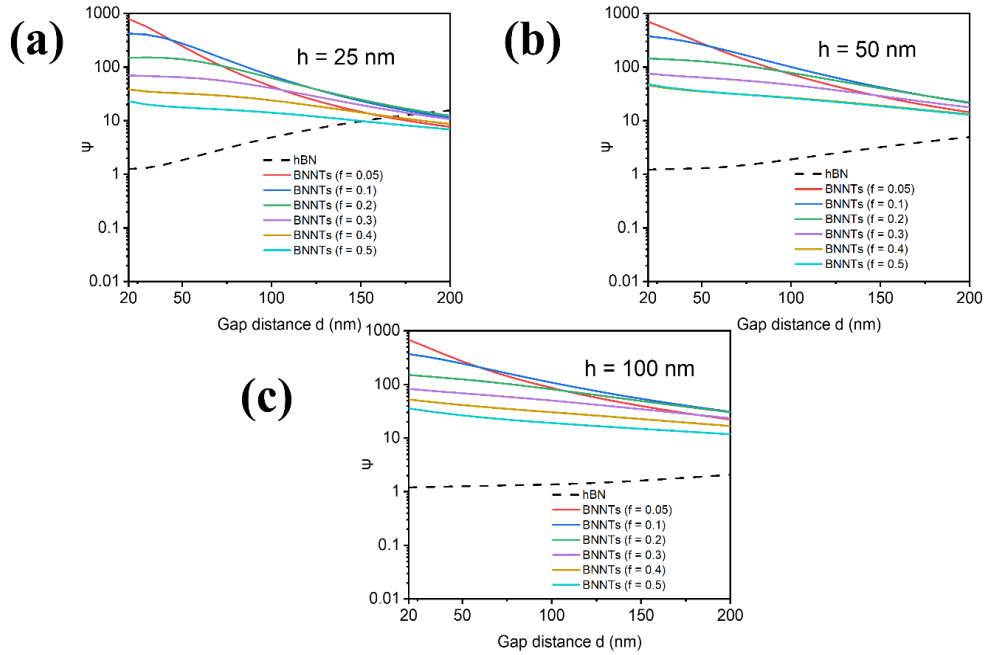

Figure 5 Spectral Allocation Ratio for hBN and BNNTs for $n_s = 1$: a) h = 25 nm b) h = 50 nm and c) h = 100 nm